

SCIENTIFIC REPORTS

OPEN

A GdAlO₃ Perovskite Oxide Electrolyte-Based NO_x Solid-State Sensor

Yihong Xiao, Dongmei Wang, Guohui Cai, Yong Zheng & Fulan Zhong

Received: 20 March 2016
Accepted: 02 November 2016
Published: 25 November 2016

NO_x is a notorious emission from motor vehicles and chemical factories as the precursor of acid rain and photochemical smog. Although zirconia-based NO_x sensors have been developed and showed high sensitivity and selectivity at a high temperature of above 800 °C, they fail to show good performance, and even don't work at the typical work temperature window of the automotive engine (<500 °C). It still is a formidable challenge for development of mild-temperature NO_x detector or sensor. Herein, a novel amperometric solid-state NO_x sensor was developed using perovskite-type oxide Gd_{1-x}Ca_xAlO_{3-δ} (GCA) as the electrolyte and NiO as the sensing electrode. NO_x sensing properties of the device were investigated at the temperature region of 400–500 °C. The response current value at –300 mV was almost linearly proportional to the NO_x concentration between 300 and 500 ppm at 500 °C. At such a temperature, the optimal sensor gave the highest NO₂ sensitivity of 20.15 nA/ppm, and the maximum response current value reached 5.57 μA. Furthermore, a 90% response and 90% recover time to 500 ppm NO₂ were about 119 and 92 s, respectively. The excellent selectivity and stability towards NO_x sensing showed the potential application of the sensor in motor vehicles.

The nitrogen monoxide (NO) and nitrogen dioxide (NO₂), referred as NO_x, are one kind of the most hazardous air pollutants causing acid rain and photochemical smog¹. A major source of NO_x emission is from automobile exhaust, and as a result, the NO_x emission sharply inclined due to the rapid increase of the amount of automobiles worldwide. Therefore, detection and monitoring of NO_x gas is an important operation in environmental protection. Computerized control of internal combustion engines has improved the work efficiency and decreased the emission of NO_x gas, where the sensor tracing nitrogen oxide (NO_x) is the key to the closed loop feedback control of the emissions².

Development of NO_x sensors based on solid electrolytes has attracted great attention recently³. The solid electrolytes mainly include two categories: fluorite (AO₂)-type and perovskite (ABO₃)-type electrolyte. The traditional solid electrolytes for sensing NO_x are zirconia-based ceramics with the fluorite (AO₂)-type structure. Until recently, Yttria stabilized Zirconia (YSZ) based sensors aroused great attention due to their great sensitivity, excellent selectivity, response signal testability, simple structure, the superiority on a wide gas test range, and particularly, the operating ability under high-temperature and hazardous conditions^{4–11}. Miura *et al.*¹² fabricated an amperometric-type NO sensor using YSZ substrate with oxide electrode (CdCr₂O₄), which showed quick and selective response to NO. Park *et al.*¹³ reported a mixed-potential-type NO_x sensor using the YSZ electrolyte with a CuO electrode showing good transient responses and large response values. However, the YSZ-based sensors show high oxygen-ion conductivity only above 800 °C. The high operating temperature can lead to a series of problems such as electrode aging¹⁴, adverse reactions and interfacial diffusion between electrode and electrolyte¹⁵, weak long term stability and high cost of interconnects¹⁶ and other issues. This greatly limits the application of such sensors in NO_x detection. Therefore, it is urgent to search an alternative solid electrolyte material that can work for sensing NO_x at a mild temperature.

Recently, many mild-temperature NO_x sensors have been studied. For example, Wang *et al.*¹⁷ investigated the Pt/La₁₀Si₅NbO_{27.5} (LSNO)/NiO sensor and showed that the sensor had a very high sensitivity to NO₂ at the operating temperature of 450–600 °C. Dai *et al.*¹⁸ also fabricated an amperometric-type NO₂ sensor using Ce_{0.9}Gd_{0.1}O_{1.95} (CGO) substrated with La_{0.75}Sr_{0.25}Cr_{0.5}Mn_{0.5}O_{3-δ} (LSCM) sensing electrode, which gave the high NO₂ sensitivity of 134 nA/ppm at 500 °C. In addition, Ueda *et al.*¹⁹ reported that the electrochemical gas sensor

National Engineering Research Center of Chemical Fertilizer Catalyst (NERC-CFC), School of Chemical Engineering, Fuzhou University, Gongye Road No.523, Fuzhou 350002, Fujian, P. R. China. Correspondence and requests for materials should be addressed to F.Z. (email: zhongfulan@fzu.edu.cn)

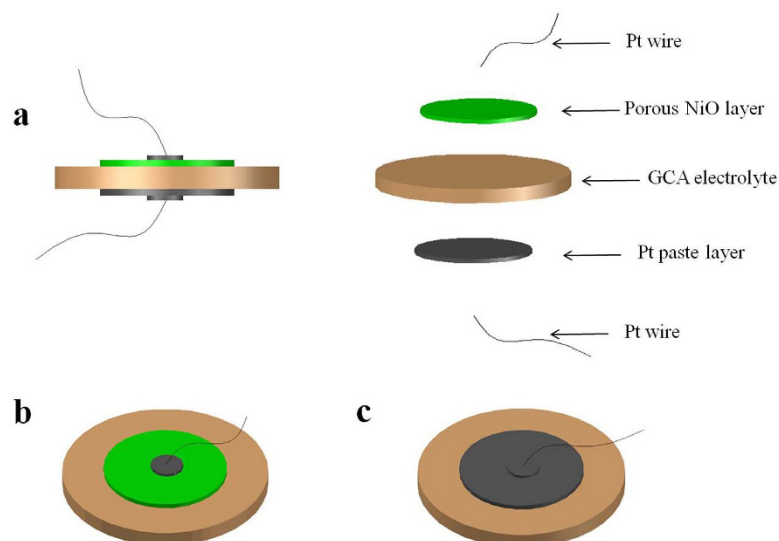


Figure 1. (a) Schematic representation of the fabricated sensor, (b) top view of the sensor, (c) bottom view of the sensor.

Pt/YSZ/La_{0.6}Sr_{0.4}Co_{0.98}Mn_{0.02}O₃, which demonstrated the fast response to NO₂ at 500–600 °C, but the response current value had only 3 μA to 400 ppm NO₂ at 550 °C.

At present, perovskite (ABO₃)-type oxides have been widely studied as potential candidates for gas sensing^{20–23}. Structurally, the AO₂ type oxides only offer A site for aliovalent ion doping. However, not only the perovskite oxides provide A site but also B site for doping, thus vacancies in the oxygen sublattice are more easily formed and the higher conductivity can be achieved. For example, the oxide ion conductivity exhibiting in the doubly-doped La_{0.8}Sr_{0.2}Ga_{0.83}Mg_{0.17}O_{2.815} (LSGM) perovskite oxide is three times higher than 8YSZ at 800 °C^{24,25}. Sinha *et al.*²⁶ showed that calcium-doped GdAlO₃ is promising material for oxygen-ion-conducting solid electrolyte application. Among the doped systems, Gd_{0.85}Ca_{0.15}AlO_{3–δ} showed a conductivity of 0.057 S/cm at 1000 °C, which was only slightly less than that of yttria-stabilized zirconia at the same temperature. Moreover, the gadolinium aluminate material was widely applied in different luminescent display systems^{27–31}, neutron absorption, and control rod^{32–36}. It was also reported that the gadolinium aluminate material could be applied to the solid oxide fuel cell^{37,38}. However, to the best of our knowledge, no reports were found on NO_x sensors that are prepared using calcium-doped GdAlO₃ system as solid electrolyte.

In this paper, an amperometric NO_x sensor was fabricated using perovskite-type oxide Gd_{1–x}Ca_xAlO_{3–δ} (GCA) as an electrolyte, NiO as sensing electrode (NiO-SE), and a noble metal Pt as reference electrode (Pt-RE), as illustrated in Fig. 1. The GCA powder was synthesized by citrate gel route. The advantage of citrate gel route over the conventional solid-state synthesis method, particularly for singly and doubly doped GdAlO₃ compositions, is that it tunes at a molecular level and produces solid powders that could be sintered to have good densities at significantly lower temperatures³⁹. NO₂ sensing performance of the device was measured on the Electrochemical Workstation to study its sensitivity, selectivity and stability at the temperature range of 400–500 °C.

Results and Discussion

Characterization of the sensor materials. XRD patterns and an expanded view around 2θ (33.6–34.4°) of the samples calcined at 1500 °C for 4 h are shown in Fig. 2A and B, respectively. As shown in Fig. 2A, when x was in the range of 0–0.1, the diffraction peaks of the resulting samples were indexed to orthorhombic crystal structure of GdAlO₃ phase [ICDD PDF 46–0395]. However, for $x = 0.15$ and 0.2, additional diffraction peaks were observed in the XRD patterns, indicating the emergence of a impurity phase indexed to the tetragonal crystal structure of GdCaAl₃O₇ [ICDD PDF 50–1808]. It showed that the Ca doping is limited in the GdAlO₃ lattice structure and less than 15%. The result is highly consistent with the literature²⁶. For $x = 0.05$ –0.15, it was noticed from Fig. 2B that the corresponding Bragg diffraction, 2θ , shifted towards lower values and the doublet (112, 200) was merged into a single peak.

We used the following Eq. 1 for further analyzing the measured XRD patterns. Based on the {110}, {112}, and {024} peaks, the lattice parameters for a given symmetry can be calculated as shown in Fig. S1. The Ca doping at $x = 0.05$ does not change a value, whereas b decreases significantly from 8.49 Å to 5.95 Å and c increases from 6.47 Å to 7.47 Å. With increasing the Ca²⁺ concentration to 15%, these lattice parameters don't further change, indicating that the Ca²⁺ doping only resulted in the d_{hkl} expansion. Clearly, the 2θ shift to lower values was resulted from the lattice expansion. It was attributed to the difference in ionic size because the Ca²⁺ (0.134 nm) ion was bigger than the Gd³⁺ (0.127 nm) for coordination number 12²⁶.

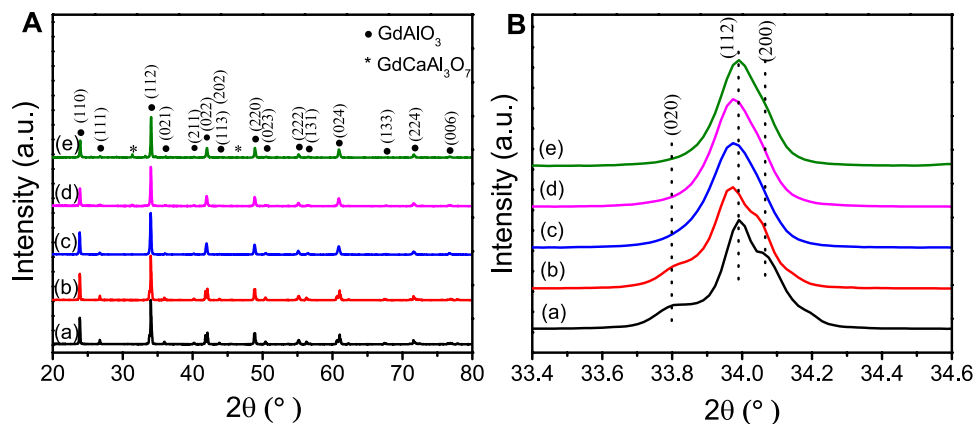


Figure 2. (A) XRD patterns of $\text{Gd}_{1-x}\text{Ca}_x\text{AlO}_{3-\delta}$ powders calcined at 1500°C for 4 h: (a) $x=0$, (b) $x=0.05$, (c) $x=0.1$, (d) $x=0.15$, (e) $x=0.2$, and (B) enlarged portion at $2\theta=33.6\text{--}34.4^\circ$.

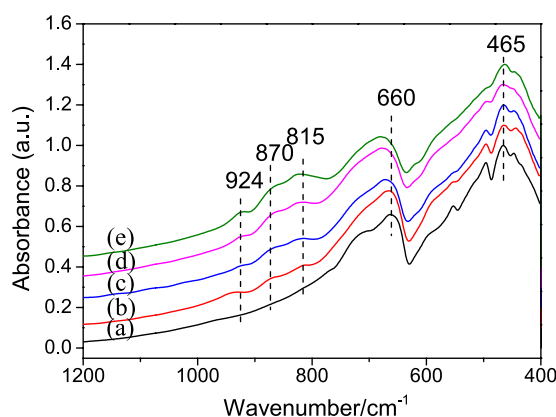


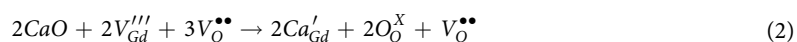
Figure 3. Infrared spectra of $\text{Gd}_{1-x}\text{Ca}_x\text{AlO}_{3-\delta}$ powders prepared by calcinations of gel precursors for 4 h at 1500°C : (a) $x=0$, (b) $x=0.05$, (c) $x=0.1$, (d) $x=0.15$, and (e) $x=0.2$.

$$n\lambda = 2d_{hkl} \sin\theta, \text{ where } d_{hkl} = \frac{1}{\sqrt{\frac{h^2}{a^2} + \frac{k^2}{b^2} + \frac{l^2}{c^2}}} \quad (1)$$

Here, n is the diffraction order, λ is the x-ray wavelength, d_{hkl} is the interplanar distance, (hkl) are the Miller indices for the corresponding d -spacing and a, b, c are the lattice parameters.

Additionally, it can be observed that with increasing x , the three peaks of $\{020, 112, 200\}$ are gradually merged into one peak and decreased in intensity. The gradual broadening and weakening are mainly originated from the lattice disordering. For $x=0.2$, the $\{112\}$ Bragg diffraction peak is nearly coincided with $x=0.0$. It was attributed to the phase change of GdAlO_3 doped with Ca^{2+} ion, leading to the formation of a new matter, $\text{GdCaAl}_3\text{O}_7$, due to the dissociation of doped Ca^{2+} ions from the GdAlO_3 lattice structure. The most different point is that the 2θ position of the $\{112\}$ peak recovers for $x=0.2$, but the broadening and weakening of these diffraction peaks are reserved, suggesting that the local structural disordering is maintained by the formation of oxygen vacancies.

Figure 3 shows the IR spectra of the samples prepared by calcinations of gel precursors for 4 h at 1500°C . It was observed that the spectra measured at different Ca-doped concentrations are basically the same except for a systematic data shift. The IR spectra showed strong bands at 660 and 465 cm^{-1} which are characteristic M-O (possibly Gd-O and Al-O stretching frequencies) vibrations for the perovskite structure compounds⁴⁰. Additionally, it was noted that the Ca-doped samples showed three new peaks at $815, 870,$ and 924 cm^{-1} and the peaks at 660 cm^{-1} moved to a higher wave number with increasing x . It has been reported that the size-induced lattice variations and the concentration of oxygen vacancies might lead to a red shift of IR absorption^{41,42}. For the $\text{Gd}_{1-x}\text{Ca}_x\text{AlO}_{3-\delta}$ systems, since the diameter size of Ca^{2+} ion is bigger than that of Gd^{3+} ion, it results in the lattice expansion and formation of oxygen vacancies. The Ca-doped GdAlO_3 point defect reaction could be written as Eq. 2²⁶:



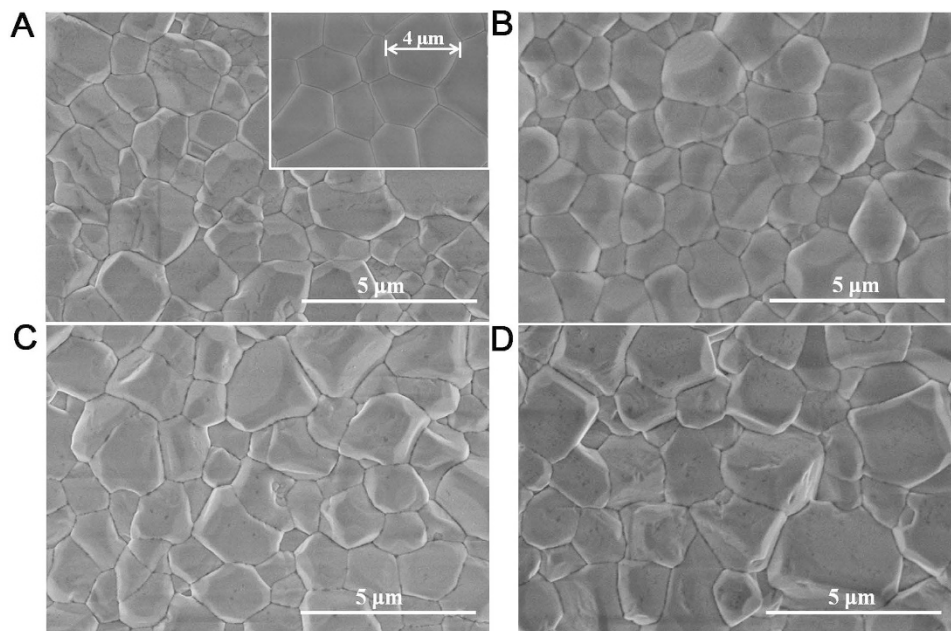


Figure 4. SEM images of the surfaces of $Gd_{1-x}Ca_xAlO_{3-\delta}$ substrates calcined at $1500\text{ }^\circ\text{C}$ for 4 h (A) $x = 0.05$, the inset shows the $x = 0$, (B) $x = 0.1$, (C) $x = 0.15$, and (D) $x = 0.2$.

Here, with increasing x , the concentration of mobile oxygen vacancies increased. Moreover, these new IR peaks are originated from the formation of some new chemical bonds by introduction of calcium. The above results suggested that Ca^{2+} ions have entered into the perovskite lattice structure.

Figure 4 shows the SEM images of surface of the $Gd_{1-x}Ca_xAlO_{3-\delta}$ substrate calcined at $1500\text{ }^\circ\text{C}$ for 4 h. The surface was consisted of microparticles with sizes between 1 and $5\text{ }\mu\text{m}$, and no open pore could be seen. The surface morphology of the undoped gadolinium aluminate sample is shown in inset of Fig. 4A. Compared to the undoped sample, it can be seen that there is no significant change in morphology and surface structure for $Gd_{1-x}Ca_xAlO_{3-\delta}$ substrates. Only the average grain sizes increased slightly with the increase of Ca doping concentration.

Sensing performance of the devices. This sensor based on the solid electrolyte substrates can be shown as the following electrochemical cells in the presence of O_2 and NO_2 : (–) $O_2 + NO_2$, NiO/GCA/Pt, $NO_2 + O_2$ (+). When the sensor was exposed to the sample gas, the response current value changed at the fixed potential of -300 mV . The following electrochemical reactions would occur at the triple-phase boundary (TPB, among gas/sensing electrode/electrolyte) and counter electrode in a series of physisorption and charge exchange reactions, as described by Eq. 3 and Eq. 4.



Amperometric response and recovery transients to $500\text{ ppm } NO_2$ with a polarized potential of -300 mV at 400 , 450 , and $500\text{ }^\circ\text{C}$ for the sensor based on $Gd_{0.85}Ca_{0.15}AlO_{3-\delta}$ substrate were shown in Fig. S2. As well known, if you choose the cathode to be positive in the software setup, and a negative voltage of -300 mV is applied in the work, you will obtain a positive current. As seen from Fig. S2, the baseline current increased with increasing temperature due to some reactions of low level impurities at electrode and slight electric conductive contribution, which was in agreement with the result reported by Wang *et al.*⁴³

Figure 5A shows the response transients of the sensor based on $Gd_{1-x}Ca_xAlO_{3-\delta}$ substrates at $500\text{ }^\circ\text{C}$ under various NO_2 concentrations in the range between 300 to 500 ppm in the presence of $5\text{ vol. } \% O_2$, when the potential of -300 mV was applied. In order to better distinguish the response curve, the base current levels have been shifted. At each NO_2 concentration, a large increase in response current value was observed in the case of the sensor based on $Gd_{1-x}Ca_xAlO_{3-\delta}$ substrate. For instance, the response current value of the sensor based on $Gd_{0.9}Ca_{0.1}AlO_{3-\delta}$ substrate was $0.93\text{ }\mu\text{A}$ for $300\text{ ppm } NO_2$ at $500\text{ }^\circ\text{C}$. When the NO_2 concentration went up to 400 ppm , the response current value inclined to $1.78\text{ }\mu\text{A}$. For the NO_2 sensor in this study, the NiO sensing electrode showed a strong adsorption and catalytic activity for NO_2 . An increase of the NO_2 concentration brought enhancement of NO_2 adsorption on the sensing electrode, which would produce more oxygen ions (O^{2-}) through the cathodic reaction of Eq. 3 and thus the response current of the sensors was improved.

In this work, the response current value was defined as the difference of current value between the sample gas and base gas ($\Delta I = |I_{gas} - I_{base}|$, where I_{gas} and I_{base} referred to the current values in the targeted concentration C ppm and $0\text{ ppm } NO_2$). Figure 5B shows the relationship between the response current of the sensor based on

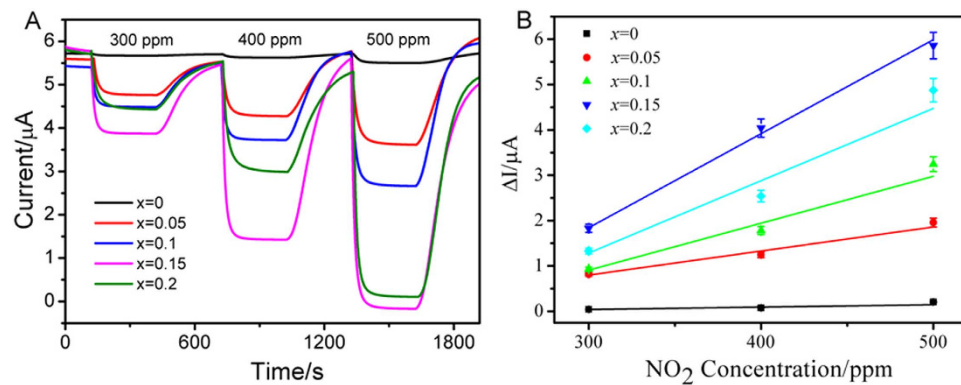


Figure 5. (A) Response transients of the sensor based on $Gd_{1-x}Ca_xAlO_{3-\delta}$ substrates to 300–500 ppm NO_2 at 500 °C in the presence of 5 vol% O_2 (applied potential -300 mV, flow rate 200 cm³/min); (B) The relationship between the response current values and NO_2 concentrations.

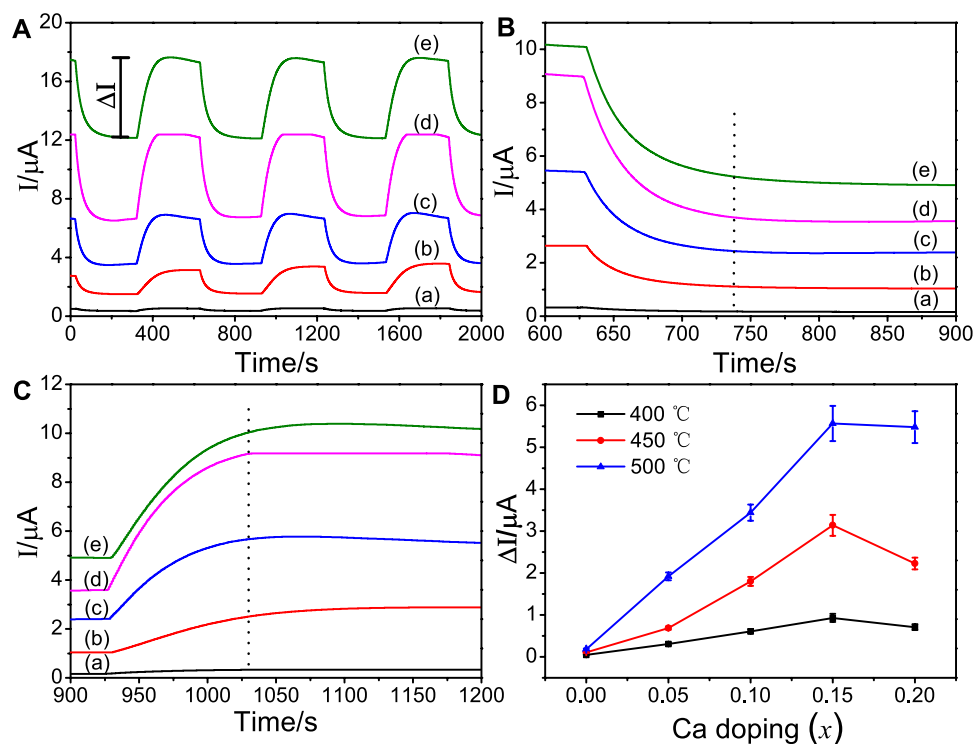


Figure 6. (A) Response transients of the sensor based on $Gd_{1-x}Ca_xAlO_{3-\delta}$ substrates to 500 ppm NO_2 in the presence of 5 vol% O_2 at 500 °C (applied potential -300 mV, flow rate 200 cm³/min): (a) $x=0$, (b) $x=0.05$, (c) $x=0.1$, (d) $x=0.15$, (e) $x=0.2$; (B) and (C) showed the enlarged portions of (A) response transients in the range between 600 to 1200 s; (D) the effect of calcium doping on the response current value of gadolinium aluminate system in 500 ppm NO_2 at 400–500 °C.

$Gd_{1-x}Ca_xAlO_{3-\delta}$ substrate and the NO_2 concentration at a bias potential of -300 mV. It can be seen that the response current value was almost linear to the NO_2 concentration from 300 to 500 ppm for the sensor based on $Gd_{1-x}Ca_xAlO_{3-\delta}$ substrate at 500 °C. The sensitivity of the sensor is defined as the ratio of response current to NO_2 concentration. For $x=0.05$ – 0.15 , the sensitivity of the sensor was enhanced with increasing the Ca doping. For example, the sensitivities of the sensors based on $Gd_{1-x}Ca_xAlO_{3-\delta}$ substrate with $x=0.05$, 0.1 and 0.15 were 5.71, 11.58 and 20.15 nA/ppm at 500 °C, respectively. Nevertheless, the sensitivity of the sensor based on the $Gd_{0.8}Ca_{0.2}AlO_{3-\delta}$ substrate declined to 19.22 nA/ppm because of over-doping. Compared to the response transient of the reference sensor based on YSZ-8 substrate to 500 ppm NO_2 in the presence of 5 vol% O_2 at 500 °C (see Supplementary Fig. S3), the sensor based on $Gd_{1-x}Ca_xAlO_{3-\delta}$ substrates showed the potential application in motor vehicles.

Figure 6A shows the response transients of the sensor to 500 ppm NO_2 at 500 °C and a bias potential of -300 mV. In order to better distinguish the response curve, the base current levels have been also shifted. It was

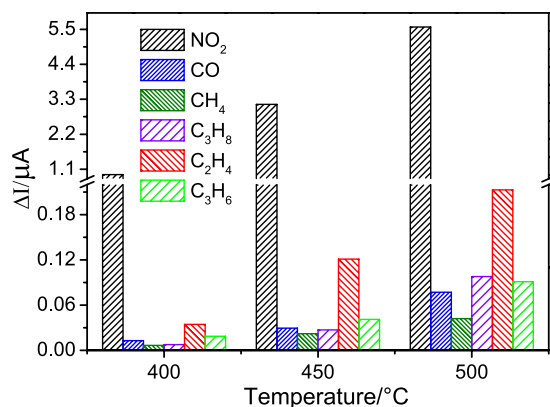


Figure 7. Selectivity of the sensor based on $\text{Gd}_{0.85}\text{Ca}_{0.15}\text{AlO}_{3-\delta}$ substrate in 500 ppm various gases at 400, 450 and 500 °C, respectively (applied potential -300 mV , flow rate $200\text{ cm}^3/\text{min}$).

observed that the response current values increased steadily from the base level upon switching from the base gas to the sample gas. The current quickly recovered to the original level when the sensor was exposed to the base gas. The response and recovery times are important parameters used to characterize a sensor. The response time is defined as the time that the resistance of the sensor reaches to 90% of the saturation value when the sensor was exposed to NO_2 and the recovery time is defined as the time required for recovering 90% of the original resistance⁴⁴. The response transients in the ranges of 600–900 and 900–1200 s are shown in Fig. 6B and C, respectively. The response and recovery time initially cut down along with the Ca doping. The response time for $x = 0.05, 0.1$, and 0.15 was 136, 121 and 119 s at 500 °C, respectively. For $x = 0.2$, the response time was extended to 178 s at 500 °C. Clearly, the sensor based on $\text{Gd}_{0.85}\text{Ca}_{0.15}\text{AlO}_{3-\delta}$ substrate is the optimal device for sensing NO_2 owing to the shortest response (119 s) and recovery (92 s) time.

Figure 6D shows the effect of calcium doping on the response current values (ΔI) of the sensor based on the gadolinium aluminate system substrates at different temperatures. The current values of the undoped sample were $0.049\text{ }\mu\text{A}$ at 400 °C. With increase of Ca doping, ΔI reached 0.31, 0.61 and $0.93\text{ }\mu\text{A}$ for $x = 0.05, 0.1$, and 0.15 at 400 °C, respectively. However, ΔI of $x = 0.2$ dropped to $0.7\text{ }\mu\text{A}$, suggesting that ΔI greatly increased by doping Ca. As seen from Fig. 6D, ΔI was enhanced with increasing the operating temperature. The sensor based on $\text{Gd}_{0.85}\text{Ca}_{0.15}\text{AlO}_{3-\delta}$ substrate exhibited the highest ΔI value of $5.57\text{ }\mu\text{A}$ at 500 °C. The response currents of the Ca-doped GdAlO_3 sensors were one order magnitude higher than that of the undoped GdAlO_3 . The increase in current value may be attributed to the increased conductivity of the Ca-doped GdAlO_3 substrates. For the perovskite-type oxides, tolerance factor t , can be used for describing the relationship between symmetry and ionic radii (Eq. 5):

$$t = \frac{r_A + r_O}{\sqrt{2}(r_B + r_O)} \quad (5)$$

Here, r_A is the ionic radii of Gd^{3+} , r_B is the ionic radii of Al^{3+} , and r_O is the ionic radii of O^{2-} . Theoretically, when t is equal to 1, the orthorhombic structure of perovskite-typed GdAlO_3 will be altered to a cubic structure with a higher symmetry. The Ca doping made t approach to 1, as result of the larger ionic radius of Ca^{2+} (0.134 nm) than that of Gd^{3+} (0.127 nm) of GdAlO_3 for coordination number 12²⁶, consequently enhancing the conductivity of GdAlO_3 . Furthermore, by the Ca doping, the cell volume of the perovskite will increase and the concentration of mobile oxygen vacancies that assist the mobility of oxygen ion will increase. In brief, for $x = 0.05\text{--}0.15$, the Ca doping GdAlO_3 solid electrolyte is favorable for conductive properties of the sensor, whereas for $x = 0.2$, the conductivity begins to decrease due to the formation of impurity phase.

The selectivity is defined as the response discrepancy of an indicated gas from a mixed gas. Here, the selectivity factor is defined as $S = I_A/I_B$, where I_A and I_B are the responses of a sensor to a target gas A and an interference gas B, respectively⁴⁵. To evaluate the selectivity, the responses of the sensor based on $\text{Gd}_{0.85}\text{Ca}_{0.15}\text{AlO}_{3-\delta}$ substrate to CO , CH_4 , C_3H_8 , C_2H_4 and C_3H_6 were examined. Figure 7 shows the responses of different gases with a concentration of 500 ppm. It was observed that the sensor exhibited a high sensitivity and selectivity towards NO_2 gas compared to the other gases. The ΔI value of interference gases was fairly small in comparison with that of the sensor responding to NO_2 gas. For example, the ΔI values of NO_2 , CO , CH_4 , C_3H_8 , C_2H_4 and C_3H_6 were $5.57, 7.7 \times 10^{-2}, 4.20 \times 10^{-2}, 9.80 \times 10^{-2}, 2.13 \times 10^{-1}$, and $8.97 \times 10^{-2}\text{ }\mu\text{A}$ at 500 °C, respectively. And the selectivity factors to CO , CH_4 , C_3H_8 , C_2H_4 and C_3H_6 were 72.34, 132.62, 56.84, 26.15 and 62.10, respectively. The influence of O_2 flow on the selectivity of sensor was negligible (see Supplementary Fig. S4).

The stability of the sensor based on $\text{Gd}_{0.85}\text{Ca}_{0.15}\text{AlO}_{3-\delta}$ substrate was measured for 3 h upon exposure to 500 ppm NO_2 gas with 5 vol. % O_2 at 450 °C (Fig. 8). The horizontal shows the centerline of the response current ripple. The as-prepared sensor shows a response current (ΔI) of $5.57\text{ }\mu\text{A}$. Furthermore, after the sensor was stored for half a month, a month, and two months, the response signal decreased slightly by 2.5%, 5.0% and 7.3%, respectively. The response current decreased by about $0.43\text{ }\mu\text{A}$ after the sensor was stored in ambient atmosphere for two months, compared to the as-prepared sensor. These results suggested that the sensor had a good stability.

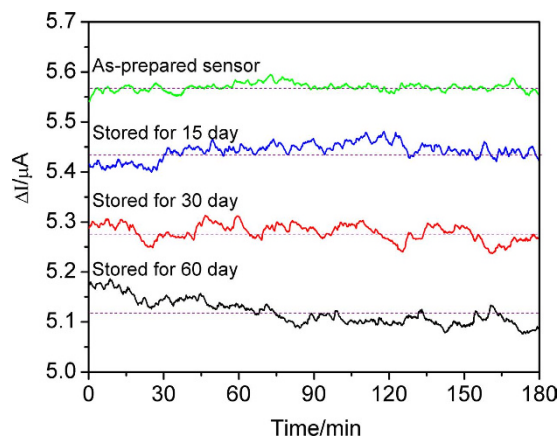


Figure 8. Stability test for the sensor based on $\text{Gd}_{0.85}\text{Ca}_{0.15}\text{AlO}_{3-\delta}$ substrate at $500\text{ }^\circ\text{C}$ in the presence of 500 ppm NO_2 (applied potential -300 mV , flow rate $200\text{ cm}^3/\text{min}$).

Conclusions

In summary, an amperometric sensor based on $\text{Gd}_{1-x}\text{Ca}_x\text{AlO}_{3-\delta}$ substrates was developed. It showed excellent sensitivity to NO_x gas at mild temperatures. The response current values of the sensor enhanced with increase of operating temperature. Furthermore, the sensitivity and response current values initially increased and then decreased with increasing the Ca doping. The $\text{Gd}_{0.85}\text{Ca}_{0.15}\text{AlO}_{3-\delta}$ sensor gave the highest NO_2 sensitivity of 20.15 nA/ppm and the highest response current value of $5.57\text{ }\mu\text{A}$ at $500\text{ }^\circ\text{C}$. Moreover, the sensor also exhibited a great selectivity and excellent stability.

Methods

Synthesis and analysis of GCA electrolytes. The Ca-doped GdAlO_3 powder was prepared through a citrate gel route^{26,39}. $\text{Gd}(\text{NO}_3)_3 \cdot 6\text{H}_2\text{O}$ (99.99% purity), $\text{Al}(\text{NO}_3)_3 \cdot 9\text{H}_2\text{O}$ (AR Grade), and $\text{Ca}(\text{NO}_3)_2 \cdot 4\text{H}_2\text{O}$ (AR Grade) were used as starting materials for preparation of $\text{Gd}_{1-x}\text{Ca}_x\text{AlO}_{3-\delta}$ (GCA) samples, where $x = 0, 0.05, 0.1, 0.15,$ and 0.2 , respectively. The starting materials were taken with composition $(\text{Gd}_{1-x}\text{Ca}_x):\text{Al} = 1:1$ molar ratio. For all the compositions, the molar ratio of total metal ion to citrate ion was kept 1. The gadolinium nitrate, aluminium nitrate and calcium nitrate were first dissolved in 250 mL distilled water at room temperature. Then citric acid as complex agent was added to the reaction solutions. Further, the mixed solution was slowly evaporated at $80\text{ }^\circ\text{C}$ under stirring to form white transparent gel. The gel was further dried at $120\text{ }^\circ\text{C}$ in an oven for 10 h to form precursor powder. After that, the powder was calcined at $1000\text{ }^\circ\text{C}$ for 4 h .

The XRD data were first recorded on a Panalytical X'Pert Pro diffractometer at 40 kV and 40 mA using $\text{Co K}\alpha_1$ ($\lambda = 0.178\text{ 901 nm}$), then revised by $\text{Cu K}\alpha_1$ ($\lambda = 0.154\text{ 056 nm}$). The samples were scanned over a 2θ range from 10° to 100° with a step size of 0.0167° at a scanning rate of $10^\circ \cdot \text{min}^{-1}$. The infrared spectra in the range of $1200\text{--}400\text{ cm}^{-1}$ were recorded on a Thermo Fisher Scientific Nicolet 6700 FTIR device. The samples were prepared as KBr pellets.

Sensor fabrication and characterization. A NO_2 sensor was fabricated using NiO as sensing electrode (NiO-SE), which was synthesized by using the sol-gel method, perovskite-type oxide $\text{Gd}_{1-x}\text{Ca}_x\text{AlO}_{3-\delta}$ as electrolyte, and a noble metal Pt as reference electrode (Pt-RE). Pellets with 8 mm in diameter and 3 mm thickness were produced by applying 150 Mpa pressure to the calcined powders, and then sintered at $1500\text{ }^\circ\text{C}$ for 4 h in the air. The NiO-SE was made from NiO paste, and a Pt wire (0.2 mm diameter) was attached to the NiO layer as a current collector. In addition, the Pt-RE was formed by using platinum paste, which was painted onto polished surface of GCA pellet which was on the other side, and then a Pt wire (0.2 mm diameter) was attached to the Pt surfaces. Subsequently, the sample was fired at $1000\text{ }^\circ\text{C}$ for 1 h in air to get the NiO/GCA/Pt sensor.

Scanning electron microscopy (SEM, HitachiS4800 instrument) was applied for observing the morphology of the samples.

Evaluation of sensing properties. The fabricated sensor was assembled in a quartz tube and the sensing properties were evaluated in a conventional gas-flow apparatus equipped with a furnace operating at temperatures in range of $400\text{--}500\text{ }^\circ\text{C}$ (see Supplementary Fig. S5). The gas environment consisted of a changing concentration of NO_2 ($0\text{--}500\text{ ppm}$) with base gases ($\text{O}_2 + \text{N}_2$ balance) at a total flow rate of $200\text{ cm}^3/\text{min}$.

The amperometric responses of the sensors were carried out using a potentiostatic method at -300 mV . The fore-mentioned electrochemical measurements were carried out by the Electrochemical Workstation (Instrument corporation of Shanghai, China, CHI600E).

References

1. Penza, M., Martucci, C. & Cassano, G. N. O_x gas sensing characteristics of WO_3 thin films activated by noble metals (Pd, Pt, Au) layers. *Sens. Actuators B*. **50**, 52–59 (1998).
2. Franklin, G. F., Powell, J. D. & Emami-Naeini, A. Feedback Control of Dynamic Systems. *Addison-Wesley world student series*. **85**, 157–175 (1994).

3. Zhuiykov, S. & Miura, N. Development of zirconia-based potentiometric NO_x sensors for automotive and energy industries in the early 21st century: what are the prospects for sensors?. *Sens. Actuators B*. **121**, 639–651 (2007).
4. Yang, J. C. & Dutta, P. K. Promoting selectivity and sensitivity for a high temperature YSZ-based electrochemical total NO_x sensor by using a Pt-loaded zeolite Y filter. *Sensor Actuat B-Chem*. **125**, 30–39 (2007).
5. Elumalai, P., Zosel, J., Guth, U. & Miura, N. NO₂ sensing properties of YSZ-based sensor using NiO and Cr-doped NiO sensing electrodes at high temperature. *Ionics*. **15**, 405–411 (2009).
6. Elumalai, P. *et al.* Tunable NO₂-Sensing Characteristics of YSZ-Based Mixed-Potential-Type Sensor Using Ni_{1-x}Co_xO-Sensing Electrode. *J. Electrochem. Soc.* **156**, J288–J293 (2009).
7. Chen, Y. & Xiao, J. Z. Synthesis of composite La_{1.67}Sr_{0.33}NiO₄-YSZ for a potentiometric NO_x sensor by microwave-assisted complex-gel auto-combustion. *Ceram. Int.* **39**, 9599–9603 (2013).
8. Miura, N. *et al.* Mixed-potential-type NO_x sensor based on YSZ and zinc oxide sensing electrode. *Ionics*. **10**, 1–9 (2004).
9. Striker, T. *et al.* Effect of nanocomposite Au-YSZ electrodes on potentiometric sensor response to NO_x and CO. *Sensor Actuat B-Chem*. **181**, 312–318 (2013).
10. Giang, H. T. *et al.* High sensitivity and selectivity of mixed potential sensor based on Pt/YSZ/SmFeO₃ to NO₂ gas. *Sensor Actuat B-Chem*. **183**, 550–555 (2013).
11. Guan, Y. Z. *et al.* Highly sensitive mixed-potential-type NO₂ sensor with YSZ processed using femtosecond laser direct writing technology. *Sensor Actuat B-Chem*. **198**, 110–113 (2014).
12. Miura, N., Lu, G., Ono, M. & Yamazoe, N. Selective detection of NO by using an amperometric sensor based on stabilized zirconia and oxide electrode. *Solid State Ion.* **117**, 283–290 (1999).
13. Park, J. *et al.* Sensing behavior and mechanism of mixed potential NO_x sensors using NiO, NiO(+YSZ) and CuO oxide electrodes. *Sensor Actuat B-Chem*. **135**, 516–523 (2009).
14. Jian, J. W., Yang, B. C. & Zhang, Y. K. Aging Characteristic of Pt/YSZ Electrode Structure. *J. Inorg. Mater.* **19**, 93–100 (2004).
15. Nguyen, T. L. *et al.* Preparation and evaluation of doped ceria interlayer on supported stabilized zirconia electrolyte SOFCs by wet ceramic processes. *Solid State Ion.* **174**, 163–174 (2004).
16. Tu, H. & Stimming, U. Advances, aging mechanisms and lifetime in solid-oxide fuel cells. *J. Power Sources*. **127**, 284–293 (2004).
17. Wang, L. *et al.* A La₁₀Si₃NbO_{27.5} based electrochemical sensor using nano-structured NiO sensing electrode for detection of NO₂. *J. Mater. Lett.* **109**, 16–19 (2013).
18. Dai, L. *et al.* Influence of process parameters on the sensitivity of an amperometric NO₂ sensor with La_{0.75}Sr_{0.25}Cr_{0.5}Mn_{0.5}O_{3-δ} sensing electrode prepared by the impregnation method. *J. Ceram. Int.* **41**, 3740–3747 (2015).
19. Ueda, T. *et al.* Zirconia-based amperometric sensor using La-Sr-based perovskite-type oxide sensing electrode for detection of NO₂. *J. Electrochem Commun.* **11**, 1654–1656 (2009).
20. Ishihara, T. *et al.* Potentiometric oxygen sensor operable in low temperature by applying LaGaO₃-Based oxide for electrolyte. *J. Electrochem. Soc.* **144**, L122–L125 (1997).
21. Dutta, A., Ishihara, T. & Nishiguchi, H. An Amperometric Solid-State Gas Sensor Using a LaGaO₃-Based Perovskite Oxide Electrolyte for Detecting Hydrocarbon in Exhaust Gas. A Bimetallic Anode for Improving Sensitivity at Low Temperature. *Chem. Mater.* **16**, 5198–5204 (2004).
22. Gu, Y. Y. *et al.* Research on the Sensing Characteristics of Amperometric NO₂ Sensor Based on La_{0.9}Sr_{0.1}Ga_{0.8}Mg_{0.2}O_{3-δ}. *Chin. J. Sens. Actuators*. **25**, 1631–1635 (2012).
23. He, B. G., Liu, T. & Cheng, C. Preparation and Property of Limiting Current Oxygen Sensor with Sr_{0.9}Y_{0.1}CoO_{3-δ} Dense Diffusion Barrier Layer. *J. Chin. Ceram. Soc.* **42**, 268–274 (2004).
24. Huang, K., Tichy, R. S. & Goodenough, J. B. Superior Perovskite Oxide-Ion Conductor; Strontium- and Magnesium-Doped LaGaO₃: I, Phase Relationships and Electrical Properties. *J. Am. Ceram. Soc.* **81**, 2565–2575 (1998).
25. Huang, K., Tichy, R. S., Goodenough, J. B. & Milliken, C. Superior Perovskite Oxide-Ion Conductor; Strontium- and Magnesium-Doped LaGaO₃: III, Performance Tests of Single Ceramic Fuel Cells. *J. Am. Ceram. Soc.* **81**, 2581–2585 (1998).
26. Sinha, A., Sharma, B. P. & Gopalan, P. Development of novel perovskite based oxide ion conductor. *Electrochim. Acta*. **51**, 1184–1193 (2006).
27. Andreetta, J. P. & Jovanic, B. R. Growth and optical properties of Cr³⁺ doped GdAlO₃ single crystals. *Mater. Res.* **3**, 45–49 (2000).
28. Raju, G. S. R. *et al.* Synthesis and luminescent properties of low concentration Dy³⁺: GAP nanophosphors. *Opt. Mater.* **31**, 1210–1214 (2009).
29. Jin, Y. P. *et al.* Enhanced green emission from Tb³⁺-Bi³⁺ co-doped GdAlO₃ nanophosphors. *Mater. Res. Bull.* **45**, 572–575 (2010).
30. Raju, G. S. R. *et al.* Synthesis, structural and luminescent properties of Pr³⁺ activated GdAlO₃ phosphors by solvothermal reaction method. *Curr. Appl. Phys.* **11**, S292–S295 (2011).
31. Jisha, P. K. *et al.* Facile combustion synthesized orthorhombic GdAlO₃:Eu³⁺ nanophosphors: Structural and photoluminescence properties for WLEDs. *J. Lumin.* **163**, 47–54 (2015).
32. Machida, M., Yada, M., Ohya, M. & Kijima, T. Synthesis of porous yttrium aluminium oxide templated by dodecyl sulfate assemblies. *Chem. Commun.* **18**, 1941–1942 (1998).
33. Malinowski, M. *et al.* Spectroscopy and upconversion processes in YAlO₃:Ho³⁺ crystals. *Opt. Mater.* **12**, 409–423 (1999).
34. Nieminen, M. *et al.* Surface-controlled growth of LaAlO₃ thin films by atomic layer epitaxy. *J. Mater. Chem.* **11**, 2340–2345 (2001).
35. Tall, P. D., Coupeau, C. & Rabier, J. Indentation-induced twinning in LaAlO₃ single crystals: An atomic force microscopy study. *Scripta Mater.* **49**, 903–908 (2003).
36. Chroma, M. *et al.* Processing and characterization of sol-gel fabricated mixed metal aluminates. *Ceram. Int.* **31**, 1123–1130 (2005).
37. Sinha, A., Näfe, H., Sharma, B. P. & Gopalan, P. Effect of electrode polarisation on the determination of electronic conduction properties of an oxide ion conductor. *Electrochim. Acta*. **55**, 8766–8770 (2010).
38. Liu, G. H., Wang, F. & Yan, R. Q. Applicability of Gd_{0.9}Ca_{0.1}AlO_{3-δ} ceramic electrolyte for intermediate temperature solid oxide fuel cells. *Adv. Mater. Res.* **476–478**, 1785–1789 (2012).
39. Sinha, A., Näfe, H., Sharma, B. P. & Gopalan, P. Synthesis of gadolinium aluminate powder through citrate gel route. *J. Alloys Comp.* **502**, 396–400 (2010).
40. Cizauskaite, S. *et al.* Sol-gel preparation and characterization of gadolinium aluminate. *Mater. Chem. Phys.* **102**, 105–110 (2007).
41. Lu, L., Liu, L. P., Wang, X. J. & Li, G. S. Understanding of the finite size effects on lattice vibrations and electronic transitions of nano alpha-Fe₂O₃. *J. Phys. Chem. B*. **109**, 17151–17156 (2005).
42. Zheng, Y. H. *et al.* Luminescence and photocatalytic activity of ZnO nanocrystals: correlation between structure and property. *Inorg. Chem.* **46**, 6675–6682 (2007).
43. Wang, L., Han, B. X., Dai, L., Zhou, H. Z. & Li, Y. H. An amperometric NO₂ sensor based on La₁₀Si₃NbO_{27.5} electrolyte and nano-structured CuO sensing electrode. *J. Hazard. Mater.* **262**, 545–553 (2013).
44. Raut, B. T. *et al.* Development of nanostructured CdS sensor for H₂S recognition: structural and physical characterization. *J. Mater. Sci.- Mater. Electron.* **23**, 956–963 (2012).
45. Nalage, S. R., Chougule, M. A., Sen, S. & Patil, V. B. Novel method for fabrication of NiO sensor for NO₂ monitoring. *J. Mater. Sci.- Mater. Electron.* **24**, 368–375 (2013).

Acknowledgements

This work was financially supported by National Science Foundation of China (Grants No. 21403035), Natural Science Foundation of Fujian Province, China (Grants No. 2015J01051), and Fujian Provincial Department of Education of Manufacturing, Education and Research project of China (Grants No. JA12023).

Author Contributions

Yihong Xiao and Fulan Zhong conceptualized the idea and device design. Dongmei Wang and Fulan Zhong performed the experiments and the data analysis. Dongmei Wang wrote the main manuscript text. Guohui Cai and Yong Zheng involved in correction of the manuscript. All the authors discussed the results and reviewed the manuscript.

Additional Information

Supplementary information accompanies this paper at <http://www.nature.com/srep>

Competing financial interests: The authors declare no competing financial interests.

How to cite this article: Xiao, Y. *et al.* A GdAlO₃ Perovskite Oxide Electrolyte-Based NO_x Solid-State Sensor. *Sci. Rep.* **6**, 37795; doi: 10.1038/srep37795 (2016).

Publisher's note: Springer Nature remains neutral with regard to jurisdictional claims in published maps and institutional affiliations.



This work is licensed under a Creative Commons Attribution 4.0 International License. The images or other third party material in this article are included in the article's Creative Commons license, unless indicated otherwise in the credit line; if the material is not included under the Creative Commons license, users will need to obtain permission from the license holder to reproduce the material. To view a copy of this license, visit <http://creativecommons.org/licenses/by/4.0/>

© The Author(s) 2016